

Nature of electro-optic response in tetragonal BaTiO₃

Inhwan Kim , Therese Paoletta, and Alexander A. Demkov ^{*}
 Department of Physics, The University of Texas, Austin, Texas 78712, USA

 (Received 15 June 2023; revised 7 August 2023; accepted 29 August 2023; published 11 September 2023)

Barium titanate, BaTiO₃ (BTO), has emerged as a promising electro-optic material with applications in silicon photonics. It boasts one of the largest known electro-optic coefficients; however, the origin of this giant electro-optic response has not been investigated in detail and is poorly understood. Here we report on a first-principles study of the electro-optic or Pockels tensor in tetragonal $P4mm$ BTO. We find good agreement with experiment if the $P4mm$ structure is viewed as a dynamic average of four lower symmetry Cm structures. The large value of the Raman component of the EO coefficient is attributed to a low frequency and strong electron-phonon coupling of the lowest optical mode, and we trace the equally large piezoelectric contribution to the large components of the piezoelectric and elasto-optic tensors.

DOI: [10.1103/PhysRevB.108.115201](https://doi.org/10.1103/PhysRevB.108.115201)

I. INTRODUCTION

As integrated silicon photonics (SiPh) experiences a revolution, one of the key tasks is the development of compact high-performance optical modulators [1]. Phase shifters using the linear electro-optic (EO) effect offer an attractive option for building such devices. Bulk silicon does not exhibit significant EO activity (the linear Pockels effect is forbidden by symmetry and the Kerr effect is rather small), so new EO materials compatible with Si and methods that can leverage the existing silicon fabrication infrastructure are being vigorously explored [2]. Recently, strained silicon and other materials have been implemented in EO modulators in SiPh, providing competitive speed, broad bandwidth, and low power consumption [3–6]. The Pockels effect, describing the change in the refractive index under an applied electric field, offers an excellent path to building even more efficient phase shifters, but it requires heterogeneous integration [7]. One of the highest known Pockels responses is reported for the tetragonal phase of BTO [8]. Indeed, recently, BTO has been successfully integrated onto SiPh platforms to fabricate EO modulators based on the Pockels effect [9], showing tremendous promise. BTO has also been epitaxially integrated onto several semiconductor substrates in addition to Si, such as Ge and GaAs, making it an even more versatile materials platform [2,10]. The range of emergent applications of Si-integrated-BTO films includes intrachip data transmission [11], neuromorphic logic optical chips [12], and photonic integrated circuits [13–15].

Traditionally, the most common use of the Pockels effect has been in the telecommunications industry, where optical modulators are fabricated from lithium niobate LiNbO₃ (LN) [16]. The effective Pockels coefficient of ~ 30 pm/V for LN sets a “gold standard” for an appreciable Pockels response [17]. Additionally, LN’s broad spectral range also makes it

attractive compared to other EO materials [18]. Some materials exhibit stronger responses, yet they are thermally and chemically unstable under conditions needed for integration with silicon photonics [19]. BTO, on the other hand, has a much stronger Pockels response (~ 1300 pm/V [8]), is chemically and thermally stable, can be monolithically integrated on silicon (001) used in complementary metal oxide semiconductor technology, and has already been demonstrated in a variety of applications, including SiPh [20–22].

Ab initio theoretical modeling is an indispensable tool in modern materials design. A deeper physical understanding of the EO response in tetragonal BTO through a detailed theoretical analysis would undoubtedly aid in developing a more efficient modulator. Unfortunately, due to the large lattice anharmonicity, tetragonal BTO exhibits imaginary phonon frequencies (and thus dynamic instability) in traditional zero Kelvin density functional theory (DFT) calculations, making the direct calculation of the EO response impossible. The harmonic approximation delivers two imaginary frequencies at the Γ point in the practically important tetragonal phase (stable between 5 and 120 °C). The theory does better for a stable low temperature rhombohedral $R3m$ phase of BTO [23,24]. In principle, *ab initio* finite-temperature molecular dynamics or many-body methods can stabilize the finite temperature tetragonal phase and predict stable (real) phonon frequencies [25,26].

In this paper, we investigate the EO response of tetragonal $P4mm$ BTO. We first include the anharmonic forces via a self-consistent phonon (SCPH) calculation. However, we find that this approach does not describe the Raman (ionic) contribution to the Pockels response with sufficient accuracy as the frequency of the now stable Γ -point optical mode is too high. We trace the problem to a subtle aspect of the BTO crystal structure. The emergence of the $P4mm$ structure below the cubic-to-tetragonal Curie temperature as an average of four monoclinic Cm structures has been suggested by recent experiments [27,28]. Also, the presence of [111] Ti displacements has been reported for paraelectric cubic BTO using

^{*}demkov@physics.utexas.edu

first-principles molecular dynamics [29]. According to the authors of Refs. [27,28], the true crystal structure of tetragonal BTO with the [001] ferroelectric atomic displacement is a dynamic average of the four possible monoclinic structures with [111], [$\bar{1}$ 11], [1 $\bar{1}$ 1], and [$\bar{1}$ $\bar{1}$ 1] Ti displacements. Here we explore this conjecture using first-principles calculations with the primary goal of understanding the EO response. When we consider this averaged atomic structure, we compute not only the stable optical modes, but both the ionic and piezo parts of the Pockels tensor in good agreement with experiment. The rest of the paper is organized as follows. First, we discuss the structural considerations and provide the necessary theoretical background related to the computation. We then provide a detailed analysis of the microscopic origin of the EO response in tetragonal BTO, followed by conclusions.

II. BACKGROUND AND METHODS

The Pockels effect describes how the refractive index of a crystal changes under the influence of an applied electric field [30]. It is traditional to introduce it in the context of a change of the optical indicatrix as follows [31]:

$$\Delta\left(\frac{1}{n_{ij}^2}\right) = \Delta(\varepsilon^{-1})_{ij} = \sum_{\gamma} r_{ij\gamma} E_{\gamma}, \quad (1)$$

where n_{ij} is refractive index, $(\varepsilon^{-1})_{ij}$ is the inverse of the electronic dielectric tensor, $r_{ij\gamma}$ the linear electro-optic tensor (EO tensor or Pockels tensor) and i, j , and γ stand for Cartesian coordinates. It can also be written as the first-order change to the dielectric tensor induced by an applied electric field E_{γ} [32]:

$$d\varepsilon_{ij} = - \sum_{\gamma} r_{ij\gamma} \varepsilon_{ii} \varepsilon_{jj} dE_{\gamma}(\omega). \quad (2)$$

A detailed account of the density functional perturbation theory (DFPT) description of the Pockels response calculation can be found in Refs. [24,33]. Here we give only a cursory overview, relevant for this paper. In a piezoelectric material, such as BTO, the Pockels response can be broken up into three contributions: electronic, Raman or ionic, and piezoelectric. The electronic portion, $r_{ij\gamma}^{\text{elec}}$ which is proportional to $\chi_{ij}^{(2)}$, comes from the interaction of the electric field with valence electrons, assuming the ions are fixed at their equilibrium positions. It is related to the second harmonic generation effect. In perovskite oxides it is usually not very large when compared to the other two contributions. For example, in strained SrTiO₃ it is only -0.1 pm/V [34] and LiNbO₃ and KNbO₃ have the largest $r_{ij\gamma}^{\text{elec}}$ of 5.8 pm/V and 3.7 pm/V, respectively [35].

The ionic term captures the change in the dielectric tensor induced by shifts in the atomic positions in response to the applied electric field. It can be expressed as

$$r_{ij\gamma}^{\text{ion}} = - \frac{4\pi}{n_i^2 n_j^2} \sum_m \frac{1}{\omega_m^2} \left(\sum_{\kappa\alpha} \frac{\partial \chi_{ij}^{(1)}}{\partial \tau_{\kappa\alpha}} u_m(\kappa\alpha) \right) \times \left(\sum_{\kappa'\beta} Z_{\kappa'\gamma\beta}^* u_m(\kappa'\beta) \right), \quad (3)$$

where n_i is the principal refractive index, $\chi_{ij}^{(1)}$ is the linear dielectric susceptibility, and $\tau_{\kappa\alpha}$ refers to displacement of atom κ in the α direction. $Z_{\kappa'\gamma\beta}^*$ is the Born effective charge, where γ is the direction of the components of electric field, and $u_m(\kappa'\beta)$ is the eigendisplacement of mode m , describing atom κ' shifting in the β direction. ω_m is the frequency of mode m , and $\sqrt{\Omega_o}$ is the square root of the unit cell volume. More compactly, the ionic term can be written as

$$r_{ij\gamma}^{\text{ion}} = - \frac{4\pi}{\sqrt{\Omega_o} n_i^2 n_j^2} \sum_m \frac{\alpha_{ij}^m p_{m,\gamma}}{\omega_m^2}. \quad (4)$$

The expression in the first bracket of Eq. (3) is the Raman susceptibility α_{ij}^m divided by $\sqrt{\Omega_o}$. It describes the modulation of the linear susceptibility $\chi^{(1)}$ by atomic vibrations [36]. The second bracket is the mode polarity $p_{m,\gamma}$ that describes the dipole moment of a mode.

The piezoelectric contribution is the third piece of the Pockels tensor; it describes the effect of strain caused by the converse piezoelectric effect. If the frequency of the applied electric field is sufficiently high, the EO response will be ‘‘clamped,’’ referring to the lattice vectors staying fixed. We assume the applied field frequency is low enough to trigger the converse piezoelectric effect. Thus, we compute the unclamped response, which can be written in terms of the clamped Pockels tensor $r_{ij\gamma}^{\eta}$, the piezoelectric strain coefficients $d_{\gamma\mu\nu}$, and elasto-optic coefficients $p_{ij\mu\nu}$:

$$r_{ij\gamma}^{\sigma} = r_{ij\gamma}^{\eta} + \sum_{\mu,\nu=1}^3 p_{ij\mu\nu} d_{\gamma\mu\nu}. \quad (5)$$

The piezoelectric strain coefficients can be calculated directly using first-principles software packages such as ABINIT (see below). However, the elasto-optic coefficients must be calculated ‘‘by-hand’’. They are defined as the derivatives of the inverse dielectric tensor with respect to strain. We can rewrite the second term of Eq. (5) in terms of the inverse dielectric tensor and convert the derivative into a finite-difference form:

$$\Delta(\varepsilon^{-1})_{ij}^{\text{piezo}} = \sum_{\mu,\nu=1}^3 p_{ij\mu\nu} \eta_{\mu\nu}, \quad (6)$$

$$p_{ij\mu\nu} \approx \frac{\Delta(\varepsilon^{-1})_{ij}(\eta^+) - \Delta(\varepsilon^{-1})_{ij}(\eta^-)}{2\eta_{\mu\nu}} + \mathcal{O}(\eta^2). \quad (7)$$

$\eta_{\mu\nu}$ is the (μ,ν) element of the strain tensor describing the lattice distortion due to the electric field. We give a definition of strain for the purpose of this calculation in Appendix. Following the methods of previous studies [37], $p_{ij\mu\nu}$ is obtained by finite difference. First, the high-frequency dielectric tensor is calculated in the equilibrium configuration. Then the lattice vectors are strained, and the internal coordinates relax in this new unit cell. For the shear component of the elasto-optic coefficient p_{2323} (p_{44} in the Voigt notation), we apply the shear strain η_{23} to the cell and do not relax the internal coordinates. We compute the dielectric tensor for unit cells under different strain values, then evaluate Eq. (7) using a centered, finite-difference derivative with respect to parametrized strain.

All calculations are performed within the framework of DFT, using the ABINIT [33,38,39] and VASP [40–45] soft-

ware packages. In ABINIT, the Ceperley-Alder local density approximation [46,47] was used to calculate the exchange-correlation energy. We use norm-conserving pseudopotentials with valence electron configurations $5s^2 5p^6 6s^2$ for the barium atom (s and p electrons included as semicore states), $3s^2 3p^6 4s^2 3d^2$ for the titanium atom, and $2s^2 2p^4$ for the oxygen atoms [48]. We achieved convergence of 1×10^{-5} eV/atom with a cutoff energy of 1600 eV and a $12 \times 12 \times 12$ Monkhorst-Pack k -point grid. Following Veithen *et al.* [33], we adopt the $2n + 1$ theorem and use DFPT to calculate the clamped Pockels tensor. The details of the theory can be found in [24,33]. Using the formulation implemented in ABINIT, we are able to compute all the terms needed to construct the Pockels tensor, including the Raman susceptibility, phonon frequencies and displacement patterns, and mode polarities. For the SCPH calculation at finite temperature, we considered $2 \times 2 \times 2$ supercell structures of the primitive BTO lattice of the $P4mm$ phase to reduce the computational cost. The forces were converged to less than 1×10^{-7} eV/atom. The second-, third-, and fourth-order anharmonic interatomic force constants are considered using the SCPH software ALAMODE [26]. As ABINIT does not support ALAMODE, we have used VASP for this calculation. In VASP, we use projected augmented wave potentials with valence electron configurations $5s^2 5p^6 6s^2$ for the barium atom (s - and p -electrons included as semicore states), $3s^2 3p^6 4s^2 3d^2$ for the titanium atom, and $2s^2 2p^4$ for the oxygen atoms [47]. We reach convergence of 1×10^{-5} eV/atom using a plane-wave cutoff energy of 600 eV and a $12 \times 12 \times 12$ Monkhorst-Pack k -point grid [49]. We find that for $P4mm$ BTO, ALAMODE gives phonon frequencies at the Γ point similar to those reported using another SCPH software, SCAILD [50,51].

III. RESULTS AND DISCUSSION

Before considering the ionic part of the Pockels tensor, let us discuss the structure of tetragonal BTO that we have used in this paper in more detail. In the ferroelectric atomic displacement pattern of the tetragonal $P4mm$ phase, the titanium and oxygen atoms exhibit opposite displacements along the z direction (the [001] direction, coinciding with the c axis of the cell), giving the cell its spontaneous ferroelectric polarization. However, recent experimental reports suggest that Ti displacement is not really in the [001] direction but is rather an average of four [111], $[\bar{1}\bar{1}1]$, $[1\bar{1}\bar{1}]$, and $[\bar{1}\bar{1}\bar{1}]$ displacements [27,28]. Each one of these configurations with a [111]-type displacement is monoclinic, with Cm space group. If the crystal rapidly samples these four configurations, on average, the structure appears to have $4mm$ space group symmetry, as if [001] was the direction of displacement. Thus, in this study, after failing to adequately describe the relevant phonon mode using many-body renormalization (see below), we consider all four monoclinic Cm BTO configurations with the [111]-type displacement. We start with the tetragonal cell with the initial [111] displacement of Ti and fully relax the atomic coordinates. The atomic positions for the optimized $P4mm$ and the Cm configurations are listed in Table I. The displacement in the Cm cell is not precisely along [111], but we will call it that for simplicity. We find that the Cm configuration gives stable

TABLE I. Fractional atomic coordinates for $P4mm$ and Cm BaTiO₃.

Element	$P4mm$			Cm		
	x	Y	z	x	y	z
Ba	0	0	0	0	0	0
Ti	0.5	0.5	0.513	0.507	0.507	0.513
O ₁	0	0.5	0.487	0	0.494	0.488
O ₂	0.5	0	0.487	0.494	0	0.488
O ₃	0.5	0.5	0.98	0.495	0.495	0.981

phonon modes and is lower in energy when compared to the original [001] $P4mm$ structure.

Some care needs to be taken when considering the cell volume. The tetragonal phase of BTO is observed at room temperature, and our optimization is performed at zero Kelvin [52]. We consider a slightly expanded volume of the Cm cell to take thermal expansion into account. To estimate the thermal expansion we used experimental data interpolated for a pseudocubic cell [53]. Starting with the theoretical minimum, we gradually expanded the volume, keeping the experimental c/a ratio, until the cell volume is 1.02 times larger than the theoretically optimized one while checking for dynamic stability along the way. After stabilizing the Cm configuration, we find the lowest stable optical phonon frequency at the Γ point to be 17 cm^{-1} (the reported experimental value is 34 cm^{-1} [54]). We then use this Cm configuration to calculate the EO tensor for tetragonal BTO. The values of the tensor components for the $P4mm$ cell are computed by averaging the values computed for the four Cm cells (see Fig. 1).

We have also investigated the energy barrier to changing the direction of the polarization of the Cm configuration using a nudged elastic band (NEB) method. In the NEB calculation, a series of “images” is produced by linearly interpolating between the initial and final states. The images, or sets of coordinates and lattice vectors, are connected by “springs,” which figure in the optimization toward the most likely path across the adiabatic potential energy surface from the initial to final state [55]. We use VASP in our NEB calculations. For all energy paths, the initial configuration is the Cm cell with polarization pointing in the [111] direction. The final state

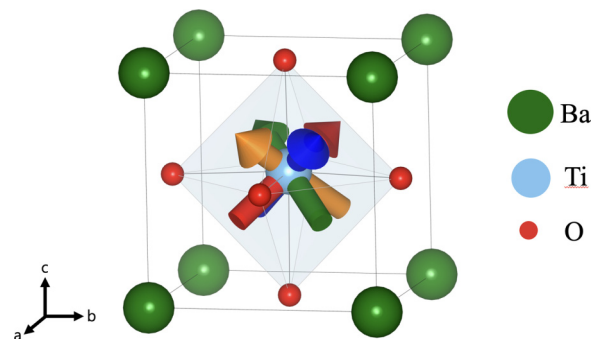


FIG. 1. Ball and stick model of [111]-displacement type monoclinic Cm BaTiO₃. The different colors of the arrows represent the [111], $[\bar{1}\bar{1}\bar{1}]$, $[1\bar{1}\bar{1}]$, and $[\bar{1}\bar{1}1]$ displacements that are averaged in the tetragonal $P4mm$ BaTiO₃.

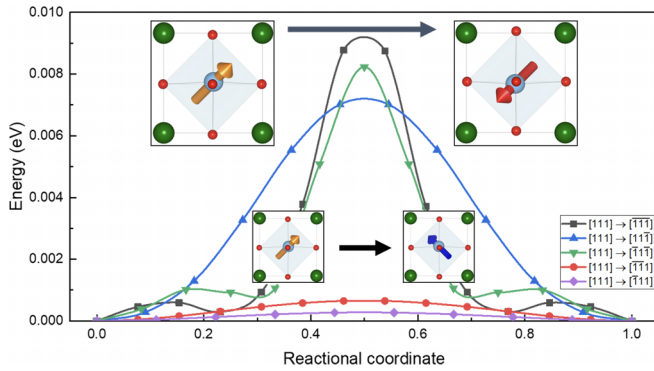


FIG. 2. The energy barriers for the polarization switching from the $[111]$ direction (reaction coordinate = 0) to other possible directions (reaction coordinate = 1) in a Cm cell with a c/a ratio of 1.007. There are five different ways to change polarization. Three paths lead to the polarization switching from an “up” to “down” configuration. And two paths correspond to switching between four possible “up” configurations. The energy barrier is more than an order of magnitude lower for the transitions that do not change the “polarity.”

can be the same cell with polarization pointing “down” in the $[1\bar{1}\bar{1}]$, $[\bar{1}\bar{1}\bar{1}]$, $[\bar{1}\bar{1}\bar{1}]$, or $[\bar{1}\bar{1}\bar{1}]$ directions, alternatively it may correspond to switching polarization between the four possible upward directions ($[111]$, $[1\bar{1}1]$, $[\bar{1}11]$, and $[\bar{1}\bar{1}1]$). Since the $[\bar{1}\bar{1}\bar{1}]$ state is the same as the $[\bar{1}\bar{1}\bar{1}]$ state and the $[1\bar{1}\bar{1}]$ state is the same as the $[\bar{1}\bar{1}\bar{1}]$ state, there are only five different configurations for the final state. The results for the barriers are shown in Fig. 2. We see that the barrier between the structures of same polarity is small (~ 0.5 meV), consistent with the assertion that the $P4mm$ structure is a time average of these lower symmetry configurations. The barrier to switch the polarity is about 8 meV, consistent with the previously reported value of 10 meV [56].

We start our discussion with the ionic part of the Pockels tensor. As seen in Eq. (3), the ionic Pockels tensor component is a sum over the phonon modes at the Γ point; each mode’s contribution is scaled by the inverse of the square of the corresponding phonon frequency. According to Eq. (4), we need the frequency, Raman susceptibility and mode po-

larity for each mode at the Γ point. Therefore, the critical step in calculating the ionic response comes from a careful analysis of the low frequency phonon modes. These are found to be unstable in the harmonic approximation for the tetragonal $P4mm$ phase of BTO. Using the frozen-phonon method [57] we obtained the Γ point frequencies listed in Table II. We include frequencies calculated both with and without the Lydanne-Sachs-Teller (LST) correction [58], as the short-range (excluding long-range Coulomb effects described by LST) frequencies are used in the Pockels tensor calculation. Similar to previous DFT calculations [59,60], ours yielded two imaginary, degenerate frequencies. Comparing several experimental results from Raman spectroscopy [61–63], it appears that these two modes are somewhat difficult to detect. For low probing frequencies, the laser used in Raman spectroscopy interferes with detection. However, some have claimed to observe a soft E doublet at 34 cm^{-1} at 22°C , with the mode getting softer for low temperatures [54]. Consequently, we expect this lowest soft optical mode to be somewhere between 0 and 34 cm^{-1} . This may seem like a large range, but this mode’s frequency is quite sensitive to the environment (temperature [54], strain [34,60,64], etc.). To consider the effect of finite temperature, we calculate the anharmonic phonon frequencies of tetragonal BTO using the SCPH theory [26]. We include anharmonic force constants up to fourth order using the SCPH software package, ALAMODE [26,65]. We are indeed able to obtain the stable phonon modes at 300 K. However, the value of the lowest optical phonon frequency at the Γ point is 170 cm^{-1} , which is too high compared with the experimental value of 34 cm^{-1} . Similarly, a recent theoretical paper by Peng [50] considered the phonon-phonon interaction with the self-consistent *ab initio* lattice dynamics using the code SCAILD. They found the lowest optical phonon frequency of the tetragonal $P4mm$ BTO to be around 170 cm^{-1} at room temperature [50,51]. But according to Eq. (4), such a high value of the phonon frequency will render the ionic Pockels tensor far too small. This suggests that the problem may not be as simple as the anharmonic renormalization. We believe that it is structural as has been pointed out experimentally [27,28] and more recently theoretically [66].

TABLE II. Phonon frequencies at the Γ point, for each case discussed. All the transverse modes are doubly degenerate for $P4mm$ BTO. For the Cm configuration, the soft mode is not degenerate.

Mode Number	$P4mm$ SR (cm^{-1})	$P4mm$ LR (cm^{-1})	Cm SR (cm^{-1})	Cm LR (cm^{-1})	SCPH (cm^{-1})	Exp. [54] (cm^{-1})
4	$-176 i$	$-176 i$	17	57	161	34
5	$-176 i$	$-176 i$	78	170	171	180
6	164	170	170	174	174	189
7	170	170	174	175	174	
8	170	185	175	235	264	
9	287	287	236	284	281	
10	287	287	284	294	281	304
11	291	291	294	296	282	308
12	315	453	295	452	465	471
13	457	457	471	472	490	498
14	457	457	471	492	510	
15	515	718	495	674	710	725

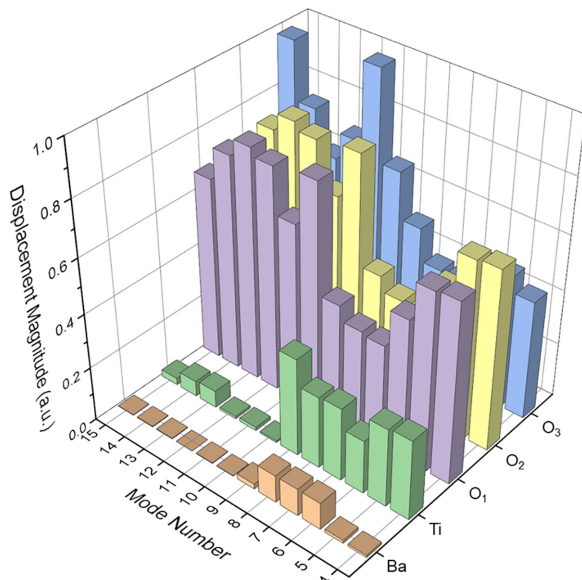


FIG. 3. Magnitude of displacement of each atom for the Γ point optical modes. Mode number 4 represents the lowest optical mode, and the mode number 15 represents the highest optical mode. Atoms 1, 2, 3, 4, and 5 represent Ba, Ti, O₁, O₂, and O₃ atoms, respectively.

The optical phonon frequencies under the different approximations for the $P4mm$ and Cm configurations at the Γ point are listed in Table II. As discussed in the previous section, the Cm cell gives a low soft mode phonon frequency at the Γ point. Therefore, in the following we will use the Cm configuration to calculate the EO tensor for BTO. The values for the tetragonal $P4mm$ symmetry are computed by averaging the values computed for the four Cm cells with the “upward” polarization.

The mode eigendisplacements also matter, as they enter the ionic Pockels contribution in both the mode polarity and Raman susceptibility calculations [see Eq. (3)]. Figure 3 shows the magnitude of the eigendisplacements of the Cm cell. Thanks to the frequency squared term in the denominator, the lowest frequency modes give the largest contributions. Compared to the previous study of the rhombohedral BTO phase (rh-BTO), the relative displacement magnitudes are similar

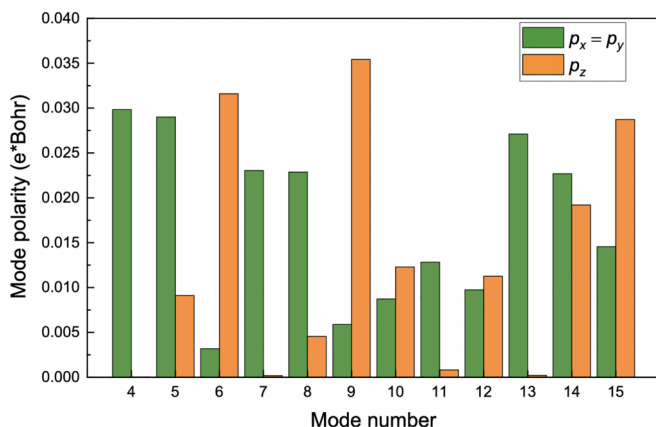


FIG. 4. Mode polarities of the Cm phase at the Γ point for each optical mode.

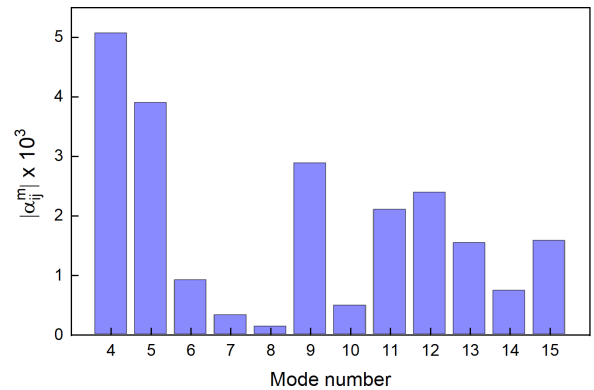


FIG. 5. The largest component of the averaged Raman susceptibility for each optical mode. Note that the lowest frequency mode, mode number 4, has the largest Raman susceptibility value among other optical modes that induces the large ionic Pockels response.

to those of rh-BTO [24], but the Cm structure has an ionic Pockels response that is about ten times larger.

Let us now discuss the mode polarity, $p_{m,y}$, that is the last bracket on the right-hand side of Eq. (3). Figure 4 shows the value of polarity for each optical mode. The x and y components have the same value for all optical modes. For the two lowest frequency modes, the polarities $p_{4,x}$ ($=p_{4,y}$), and $p_{5,x}$ ($=p_{5,y}$), are the largest. However, the mode polarity itself may not be the reason for the large value of the EO tensor of this polymorph. Previous theoretical studies have shown even larger values of the mode polarity and still obtained smaller electro-optic response compared to the current study [24,34].

The last term to consider for the ionic Pockels response is the Raman susceptibility, $\frac{\partial \chi_{ij}}{\partial \tau_{\alpha\beta}}$. To obtain $\frac{\partial \chi_{ij}}{\partial \tau_{\alpha\beta}}$, we compute the optical dielectric tensor and thus the first-order electronic susceptibility. We tested a variety of finite-difference derivatives with varying orders of accuracy and atomic displacement

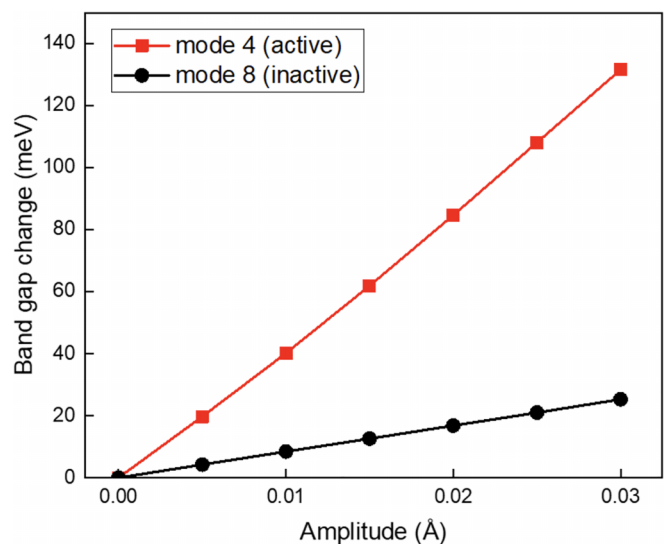


FIG. 6. Band gap change with respect to the magnitude of displacement for the Raman active (mode 4) and the inactive mode (mode 8). The Raman active displacement causes a significantly bigger change of the band gap than the Raman inactive displacement.

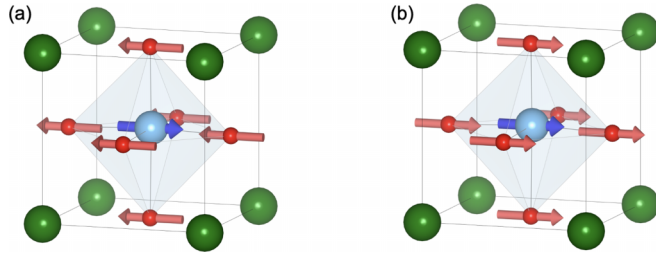


FIG. 7. The averaged eigenmode pattern of Cm phase for the (a) Raman active mode (mode 4), and the (b) Raman inactive mode (mode 8). Mode 4 shows an out-of-phase displacement pattern between Ti and O atoms, while mode 8 shows an in-phase displacement pattern, in which the bonding characteristic between Ti and O atoms barely changes.

step sizes and found a very uniform linear response. Figure 5 shows the largest component of the Raman susceptibility tensor averaged over for the four Cm configurations of the same polarity. The lowest optical mode (mode number 4), which is the Raman active mode, has the largest Raman susceptibility. Compared to the rh-BTO case, we see that rh-BTO has twice the value of α_{ij}^m for the lowest frequency mode [24]. This suggests that the critical factor determining the anomalously large ionic EO response of tetragonal BTO at room temperature is the low frequency of the optical mode.

From the electronic structure point of view the value of the Raman susceptibility is largely controlled by the sensitivity of the smallest energy difference electronic transition that is the band gap, to the mode atomic displacement [24]. To see why mode number 4 has such a large Raman susceptibility, and mode number 8 has the smallest Raman susceptibility value, we compare the band gap change in response to displacing the atoms along the eigenvectors of the corresponding modes. In Fig. 6, we plot the band gap change with respect to the amplitude. This is achieved by scaling the normalized mode eigenvector from 0 to 0.03 Å. The plot shows that the active mode opens the band gap notably, while the inactive mode barely changes the band gap.

To further understand this spectral change, we plot the phonon eigenmode pattern averaged over the four Cm configurations of the same polarity for modes 4 and 8 in Fig. 7. The Raman active mode 4, exhibits an out-of-phase displacement pattern between the Ti and O atoms along the [100] direction. This displacement changes the overlap between the titanium d states and oxygen p states. The change of the overlap results in a change of the hopping integral that, in turn, affects the magnitude of the band gap. This sensitivity leads to a large Raman susceptibility. In contrast, Raman inactive mode 8,

shows an in-phase displacement pattern, which does not affect the bonding characteristic significantly and, consequently, the Raman susceptibility is small.

The Pockels tensor is third rank; the first two indices refer to the indicatrix and the third one to the direction of the applied electric field. The tensor is symmetric in the first two indices and may be collapsed using Voigt notation. We have explored each component of the clamped Pockels response including the displacement pattern, mode polarity, and the Raman susceptibility for each mode. These quantities for each mode are combined with the optical mode frequencies (the lowest two are 17 and 78 cm^{-1}) and result in a very large r_{42}^{clamped} ($=r_{51}^{\text{clamped}}$) component of the ionic Pockels tensor. As the phonon frequency squared term is in the denominator, the lowest frequency phonon mode gives the largest ionic EO response. In Table III, we list the clamped Pockels tensor computed for each Cm cell and in Table IV we show the averaged electronic and ionic parts of the Pockels tensor consistent with $P4mm$ symmetry. Note that the large r_{42}^{clamped} value mainly comes from the ionic part. If we compare this to the experimental clamped Pockels tensor, the agreement is fair. Zgonik *et al.* report $r_{42}^{\text{clamped}} = 730$ pm/V, $r_{13}^{\text{clamped}} = 10$ pm/V, and $r_{33}^{\text{clamped}} = 40$ pm/V [67]. Both r_{13}^{clamped} , and r_{33}^{clamped} are relatively small compared to r_{42} and less important for our discussion. Recall that the ionic term is a sum over the modes, but the lowest optical phonon mode dominates r_{42}^{clamped} , providing 96% of the total ionic EO response.

Let us now discuss the piezocontribution to the Pockels response. As Eq. (5) states, the piezocontribution is a sum over the product of the piezoelectric strain tensor $d_{\gamma\mu\nu}$ and the elasto-optic tensor $p_{ij\mu\nu}$. The results of our ABINIT calculation can be found in Tables IV and V. The piezoelectric strain tensor, $d_{\gamma\mu\nu}$, is calculated by multiplying the compliance tensor, $s_{\gamma\mu\nu}$, and the piezoelectric stress tensor, $e_{m\nu}$ using the relationship between the strain and stress [30]. We first calculate the average compliance tensor and piezoelectric stress tensor to take into account four different Cm configurations. Once we average out the compliance tensor and the piezoelectric strain tensor, the $P4mm$ symmetry for those two tensors is recovered. After we get the correct symmetry, we multiply the averaged compliance tensor and the piezoelectric stress tensor to get the piezoelectric strain tensor. The only nonzero elements for the piezoelectric strain tensor are d_{13} , d_{33} , and d_{42} . Both the piezoelectric stress tensor and the compliance tensor can be directly calculated using DFPT implemented in ABINIT [33]. As one can see in Table V, the absolute values of d_{13} and d_{33} are 40 and 38 pC/N, respectively, and are comparable to the experimental values, and d_{42} , which is the most important

TABLE III. Ionic contribution to Pockels tensor r_{ij} for Cm BaTiO₃ for each displacement with the polarization “upward”.

[111]	$[\bar{1}\bar{1}\bar{1}]$	$[\bar{1}11]$	$[\bar{1}\bar{1}1]$
$\begin{bmatrix} 1812 & -1583 & -25 \\ -1584 & 1812 & -25 \\ -11 & -11 & 41 \\ -767 & 824 & -6 \\ 817 & -760 & -6 \\ 22 & 52 & -12 \end{bmatrix}$	$\begin{bmatrix} 1811 & 1582 & -25 \\ -1583 & -1810 & -25 \\ -11 & 11 & 41 \\ 767 & 824 & 6 \\ 817 & 759 & -6 \\ -22 & 52 & 12 \end{bmatrix}$	$\begin{bmatrix} -1806 & -1578 & -25 \\ 1578 & 1806 & -25 \\ 11 & -11 & 41 \\ 765 & 822 & -6 \\ 815 & 757 & 6 \\ 22 & -52 & 12 \end{bmatrix}$	$\begin{bmatrix} -1810 & 1581 & -25 \\ 1582 & -1809 & -25 \\ 11 & 11 & 41 \\ -766 & 823 & 6 \\ 816 & -758 & 6 \\ -22 & -52 & -12 \end{bmatrix}$

TABLE IV. Electronic and ionic contribution to the Pockels tensor r_{ij} , averaged to tetragonal BaTiO₃.

Electronic Pockels Tensor (pm/V)	Ionic Pockels Tensor (pm/V)
$\begin{bmatrix} 0 & 0 & 0.7 \\ 0 & 0 & 0.7 \\ 0 & 0 & 2 \\ 0 & 0.76 & 0 \\ 0.76 & 0 & 0 \\ 0 & 0 & 0 \end{bmatrix}$	$\begin{bmatrix} 1.8 & 0.5 & -25 \\ -1.8 & 0.25 & -25 \\ 0 & 0 & 41 \\ 0.25 & 823 & 0 \\ 816 & 0.5 & 0 \\ 0 & 0 & 0 \end{bmatrix}$

component for r_{42}^{piezo} element is computed to be 469 pC/N. Results of another DFPT study by Sanna and co-workers performed using the $P4mm$ structure [68] that does not describe the d_{42} well, and experimental values are included in Table V for comparison. The d_{42} element determines r_{42}^{piezo} that is significant to the total unclamped Pockels tensor value.

The last element needed for the unclamped Pockels tensor, is the elasto-optic tensor, $p_{ij\mu\nu}$. As discussed above, we calculate the elasto-optic tensor using a finite difference Eq. (7) for both Cm and $P4mm$ phases [70]. As one can see in Table VI, the Cm configuration agrees with experiment better; some components are an order of magnitude off when using $P4mm$. In particular, the p_{44} is 0.81 for the Cm configuration, while it is significantly underestimated for $P4mm$. This component is of most interest for $r_{42}^{\text{unclamped}}$. Components of the piezocontribution of the Pockels tensor are listed in Table VI. Adding together the electronic, ionic, and piezo parts of the Pockels tensor, we obtain the total unclamped Pockels tensor, $r_{42}^{\text{unclamped}} = r_{42}^{\text{clamped}} + r_{42}^{\text{piezo}} = 1564$ pm/V in reasonable agreement with the experimental value of ~ 1300 pm/V.

IV. CONCLUSIONS

We report a detailed theoretical analysis of the linear EO effect in $P4mm$ BTO, using *ab initio* calculations. We consider $P4mm$ BTO to be a dynamic average of a lower symmetry Cm structure with a [111]-type ferroelectric displacement, and find good agreement with experiment, and provide insights into the origin of BTO's uniquely large EO response. To describe tetragonal BTO, we average over four such Cm structures with the same "upward" polarization to calculate the Pockels tensor. Interestingly, neither Raman susceptibility nor the mode polarity of this phase are particularly different from those found in other BTO polymorphs, however, the small frequency of the lowest optical mode results in a very large ionic response. This particular mode boasts a winning combination of a low frequency and a displacement pattern that triggers a large change in the dielectric tensor, resulting in large Raman susceptibility. We also calculate the

TABLE V. The absolute value of piezoelectric strain tensors obtained through ABINIT, other theory [68], and experiment [67,69].

	This work	Other Theory [68]	Expt.
d_{31} (pC/N)	40	15	33 [67], 34 [69]
d_{33} (pC/N)	38	90	90 [67], 85.6 [69]
d_{42} (pC/N)	469	10	282 [67], 392 [69]

TABLE VI. Unique elements of the elasto-optic tensor (unitless) and the piezo part of the Pockels tensor.

Elasto-optic Element	Cm	$P4mm$	Expt. [67]
p_{11}	0.93	0.53	0.50
p_{12}	0.058	0.61	0.11
p_{13}	0.087	0.42	0.2
p_{31}	0.037	0.37	0.07
p_{33}	0.80	0.0085	0.77
p_{44}	0.81	0.17	1.0
r_{13}^{piezo} (pm/V)	3.5	2	-2
r_{33}^{piezo} (pm/V)	30	6	65
r_{42}^{piezo} (pm/V)	760	81	570

piezoelectric response, which is severely underestimated using the conventional $P4mm$ cell, and find good agreement with experiment. Overall, we obtain $r_{13}^{\text{unclamped}} = -20.8$ pm/V, $r_{33}^{\text{unclamped}} = 73$ pm/V, and $r_{42}^{\text{unclamped}} = 1564$ pm/V for the unclamped Pockels tensor in reasonably good agreement with experiment. Importantly, the ionic (optical phonons) and piezoresponses (strain or acoustic phonons) each account for approximately half of the total unclamped response, while the electronic component related to $\chi^{(2)}$ is relatively small and comparable to that of lithium niobate. This suggests that though the BTO EO response will diminish at frequencies above the acoustic resonance, it should still outperform lithium niobate even at high frequencies in qualitative agreement with recent experiments [71]. It also suggests that if the tetragonal phase is stabilized by suppressing the phase transition, e.g., by epitaxial strain, the material should maintain a sizable EO response at low temperature when the optical phonons are "frozen out" [24].

ACKNOWLEDGMENTS

We thank A. Posadas, M. Reynaud, and W. Li for insightful discussions and critical reading of the manuscript. We are grateful to G. Henkelman for his help with the nudged elastic band calculations. The work is supported by the Air Force Office of Scientific Research under Award No FA9550-18-1-0053.

APPENDIX: STRAIN

The elastic properties are usually derived by considering a crystal as a homogenous continuous medium rather than a periodic array of atoms [72]. One can imagine three orthogonal unit vectors, \hat{x} , \hat{y} , \hat{z} , initially embedded in the material. After a deformation, the new axes may be written in terms of the old ones:

$$\mathbf{x}' = (1 + \epsilon_{xx})\hat{x} + \epsilon_{xy}\hat{y} + \epsilon_{xz}\hat{z}, \quad (\text{A1a})$$

$$\mathbf{y}' = \epsilon_{yx}\hat{x} + (1 + \epsilon_{yy})\hat{y} + \epsilon_{yz}\hat{z}, \quad (\text{A1b})$$

$$\mathbf{z}' = \epsilon_{zx}\hat{x} + \epsilon_{zy}\hat{y} + (1 + \epsilon_{zz})\hat{z} \quad (\text{A1c})$$

The coefficients ϵ_{ij} describe the deformation with a unitless parameter measuring the relative change in magnitude of a component of the unit vector. If an atom is originally at $\mathbf{r} = x(\hat{x}) + y(\hat{y}) + z(\hat{z})$, after the lattice deforms its position

will be $\mathbf{r}' = x(\mathbf{x}') + y(\mathbf{y}') + z(\mathbf{z}')$. The displacement \mathbf{R} can then be written as

$$\mathbf{R} \equiv \mathbf{r}' - \mathbf{r} = x(\mathbf{x}' - \hat{\mathbf{x}}) + y(\mathbf{y}' - \hat{\mathbf{y}}) + z(\mathbf{z}' - \hat{\mathbf{z}}), \quad (\text{A2a})$$

$$\begin{aligned} \mathbf{R}(\mathbf{r}) \equiv & (x\epsilon_{xx} + y\epsilon_{yx} + z\epsilon_{zx})\hat{\mathbf{x}} + (x\epsilon_{xy} + y\epsilon_{yy} + z\epsilon_{zy})\hat{\mathbf{y}} \\ & + (x\epsilon_{xz} + y\epsilon_{yz} + z\epsilon_{zz})\hat{\mathbf{z}}, \end{aligned} \quad (\text{A2b})$$

$$\mathbf{R}(\mathbf{r}) = u(\mathbf{r})\hat{\mathbf{x}} + v(\mathbf{r})\hat{\mathbf{y}} + w(\mathbf{r})\hat{\mathbf{z}}. \quad (\text{A2c})$$

The coefficients of each unit vector in Eq. (A2c) comprise the sum of the first-order Taylor expansion of the difference $\mathbf{r}' - \mathbf{r}$ if we use $x\epsilon_{xx} \approx x \partial u / \partial x$, $y\epsilon_{yx} \approx y \partial u / \partial y$, etc. Using this formulation, we can actually define the strain tensor in terms of these partial derivatives. Normal strain η_{ii} , which only involves changes in the magnitude of the orthogonal unit vectors and no change in their respective angles, can be written as

$$\eta_{xx} \equiv \epsilon_{xx} = \frac{\partial u}{\partial x}; \quad \eta_{yy} \equiv \epsilon_{yy} = \frac{\partial v}{\partial y}; \quad \eta_{zz} \equiv \epsilon_{zz} = \frac{\partial w}{\partial z}. \quad (\text{A3})$$

While sheer strain η_{ij} ($i \neq j$) measures the change in the angles when the lattice vectors have been rotated toward or away from each other. This can be written in terms of the components of the rotated lattice vectors as differentials ∂u , ∂v , ∂w and the original magnitudes of the lattice vectors ∂x , ∂y , ∂z :

$$\eta_{xy} \equiv \mathbf{x}' \cdot \mathbf{y}' = \frac{1}{2}(\epsilon_{yx} + \epsilon_{xy}) = \frac{1}{2} \left(\frac{\partial u}{\partial y} + \frac{\partial v}{\partial x} \right), \quad (\text{A4a})$$

$$\eta_{yz} \equiv \mathbf{y}' \cdot \mathbf{z}' = \frac{1}{2}(\epsilon_{zy} + \epsilon_{yz}) = \frac{1}{2} \left(\frac{\partial v}{\partial z} + \frac{\partial w}{\partial y} \right), \quad (\text{A4b})$$

$$\eta_{zx} \equiv \mathbf{z}' \cdot \mathbf{x}' = \frac{1}{2}(\epsilon_{zx} + \epsilon_{xz}) = \frac{1}{2} \left(\frac{\partial u}{\partial z} + \frac{\partial w}{\partial x} \right). \quad (\text{A4c})$$

This can also be measured by finding the change in the angle between the lattice vectors (\vec{L}'_i being the new ones), assuming they were originally orthogonal [73]:

$$\eta_{ij} = \pi/2 - \cos^{-1} \left(\frac{\vec{L}'_i \cdot \vec{L}'_j}{|\vec{L}'_i| |\vec{L}'_j|} \right). \quad (\text{A5})$$

In the limit of small angles, Eqs. (A4) and (A5) are the same in a Taylor expansion. From Eqs. (A4) and (A5), one can see that the tensor η_{ij} is symmetric from the interchangeable indices. Together, Eqs. (A3)–(A5) define all the components of strain. For normal strain, the sign convention dictates that elongation be positive and compression negative. Shear strain is considered positive if the angle between lattice vectors decreases and negative if it increases. Although this may sound

counterintuitive, it ensures that positive shear stress causes positive shear strain.

In practice, we distorted the lattice vectors of the unit cell to take derivatives at the desired strain. To take derivatives with respect to normal strain, we first elongated one of the lattice vectors along the direction of its unit vector, according to Eq. (A3). For example, to consider the strain of $\eta_{xx} = 0.005$, we made the first lattice vector $\vec{L}_1 = 1.005 [3.994 \ 0 \ 0]$, keeping the other vectors constant. Then we relaxed the internal coordinates to allow for the strain-induced atomic relaxations that also affect the dielectric tensor. Once we had the new relaxed cell, we calculated the dielectric tensor for that configuration. We repeated this for $\vec{L}_1 = 0.995 [3.994 \ 0 \ 0]$. Then we could obtain the elasto-optic tensor using Eq. (7).

For shear strain, we rotated the two lattice vectors of interest toward and away from each other (positive and negative steps in the finite-derivative), according to Eqs. (A4a)–(A4c). To give the effect of $\eta_{yz} = 0.01$ strain, we rotated both the second and third lattice around the x axis. Specifically, we applied the rotation matrix \bar{M} with $\theta = -0.005$ radians to the second lattice vector \vec{L}_2 :

$$\vec{L}'_2 = \bar{M}\vec{L}_2 = \begin{pmatrix} 1 & 0 & 0 \\ 0 & \cos(-0.005) & -\sin(-0.005) \\ 0 & \sin(-0.005) & \cos(-0.005) \end{pmatrix} \begin{pmatrix} 0 \\ 3.994 \\ 0 \end{pmatrix} \quad (\text{A6})$$

to obtain $\vec{L}'_2 = [0 \ 3.99395 \ 0.01996]$. \vec{L}'_3 is obtained by a similar process:

$$\vec{L}'_3 = \bar{M}\vec{L}_3 = \begin{pmatrix} 1 & 0 & 0 \\ 0 & \cos(0.005) & -\sin(0.005) \\ 0 & \sin(0.005) & \cos(0.005) \end{pmatrix} \begin{pmatrix} 0 \\ 0 \\ 4.0038 \end{pmatrix}. \quad (\text{A7})$$

Bear in mind that the sign of θ changes to ensure they are both lattice vectors rotating toward each other. This yields $\vec{L}'_3 = [0 \ 0.02019 \ 4.03794]$. If we apply Eq. (A4a), we get

$$\begin{aligned} \eta_{yz} \equiv \mathbf{y}' \cdot \mathbf{z}' &= \epsilon_{zy} + \epsilon_{yz} = \frac{\partial v}{\partial z} + \frac{\partial w}{\partial y} \\ &= \frac{0.02019}{4.038} + \frac{0.01996}{3.994} = 0.010. \end{aligned} \quad (\text{A8})$$

Equivalently, we could apply Eq. (A5) to \vec{L}'_2 and \vec{L}'_3 to get $\eta_{yz} = 0.010$. To apply $\eta_{yz} = -0.010$, we would repeat the process, but flip the signs of θ for each rotation. After straining the lattice vectors, we relax the internal coordinates, then compute the dielectric tensor for the shear strain derivative. Thus, we are able to obtain all the elasto-optic constants.

- [1] A. Rahim, A. Hermans, B. Wohlfeil, D. Petousi, B. Kuyken, D. Van Thourhout, and R. Baets, Taking silicon photonics modulators to a higher performance level: State-of-the-art and a review of new technologies, *Adv. Photon.* **3**, 024003 (2021).
- [2] W. Guo, A. B. Posadas, and A. A. Demkov, Epitaxial integration of BaTiO₃ on Si for electro-optic applications, *J. Vac. Sci.* **39**, 030804 (2021).
- [3] G. T. Reed, G. Mashanovich, F. Y. Gardes, and D. J. Thomson, Silicon optical modulators, *Nat. Photon.* **4**, 518 (2010).

- [4] M. J. R. Heck, H. W. Chen, A. W. Fang, B. R. Koch, D. Liang, H. Park, M. N. Sysak, and J. E. Bowers, Hybrid silicon photonics for optical interconnects, *IEEE J. Sel. Top. Quantum Electron.* **17**, 333 (2011).
- [5] M. Li and H. X. Tang, Strong pockels materials, *Nat. Mater.* **18**, 9 (2019).
- [6] A. A. Demkov, C. Bajaj, J. G. Ekerdt, C. J. Palmstrøm, and S. J. B. Yoo, Materials for emergent silicon-integrated optical computing, *J. Appl. Phys.* **130**, 070907 (2021).

- [7] Y. Kim, J. H. Han, D. Ahn, and S. Kim, Heterogeneously-integrated optical phase shifters for next-generation modulators and switches on a silicon photonics platform: A review, *Micromachines* **12**, 625 (2021).
- [8] R. Boyd, *Nonlinear Optics*, 3rd ed. (Academic Press, San Diego, CA, 2008).
- [9] S. Abel, F. Eltes, J. E. Ortmann, A. Messner, P. Castera, T. Wagner, D. Urbonas, A. Rosa, A. M. Gutierrez, D. Tulli, P. Ma, B. Baeuerle, A. Josten, W. Heni, D. Caimi, L. Czornomaz, A. A. Demkov, J. Leuthold, P. Sanchis, and J. Fompeyrine, Large pockels effect in micro- and nanostructured barium titanate integrated on silicon, *Nat. Mater.* **18**, 42 (2019).
- [10] L. Mazet, S. M. Yang, S. V. Kalinin, S. Schamm-Chardon, and C. Dubourdieu, A review of molecular beam epitaxy of ferroelectric BaTiO₃ films on Si, Ge and GaAs substrates and their applications, *Sci. Technol. Adv. Mater.* **16**, 036005 (2015).
- [11] K. Yamada, Y. Urino, T. Nakamura, and Y. Arakawa, Integrated silicon-based optical interconnect for fast, compact, energy-efficient electronic circuit systems, *NTT Tech. Rev.* **11**, 1 (2013).
- [12] P. Stark, F. Horst, R. Dangel, J. Weiss, and B. J. Offrein, Opportunities for integrated photonic neural networks, *Nanophotonics* **9**, 4221 (2020).
- [13] T. D. Ladd, F. Jelezko, R. Laflamme, Y. Nakamura, C. Monroe, and J. L. O'Brien, Quantum computers, *Nature (London)* **464**, 45 (2010).
- [14] J. L. O'Brien, A. Furusawa, and J. Vučković, Photonic quantum technologies, *Nat. Photon.* **3**, 687 (2009).
- [15] J. Wang, F. Sciarrino, A. Laing, and M. G. Thompson, Integrated photonic quantum technologies, *Nat. Photon.* **14**, 273 (2020).
- [16] E. L. Wooten, K. M. Kissa, A. Yi-Yan, E. J. Murphy, D. A. Lafaw, P. F. Hallemeier, D. Maack, D. V. Attanasio, D. J. Fritz, G. J. McBrien, and D. E. Bossi, Review of lithium niobate modulators for fiber-optic communications systems, *IEEE J. Sel. Top. Quantum Electron.* **6**, 69 (2000).
- [17] D. Janner, D. Tulli, M. García-Granda, M. Belmonte, and V. Pruneri, Micro-structured integrated electro-optic LiNbO₃ modulators, *Laser Photon. Rev.* **3**, 301 (2009).
- [18] M. Leidingner, S. Fieberg, N. Waasem, F. Kühnemann, K. Buse, and I. Breunig, Comparative study on three highly sensitive absorption measurement techniques characterizing lithium niobate over its entire transparent spectral range, *Opt. Express* **23**, 21690 (2015).
- [19] A. Rahim, T. Spuesens, R. Baets, and W. Bogaerts, Open-access silicon photonics: Current status and emerging initiatives, *Proc. IEEE* **106**, 2313 (2018).
- [20] K. J. Kormondy, S. Abel, F. Fallegger, Y. Popoff, P. Ponath, A. B. Posadas, M. Sousa, D. Caimi, H. Siegwart, E. Uccelli, L. Czornomaz, C. Marchiori, J. Fompeyrine, and A. A. Demkov, Analysis of the pockels effect in ferroelectric barium titanate thin films on Si(001), *Microelectron. Eng.* **147**, 215 (2015).
- [21] C. Dubourdieu, J. Bruley, T. M. Arruda, A. Posadas, J. Jordan-Sweet, M. M. Frank, E. Cartier, D. J. Frank, S. V. Kalinin, A. A. Demkov, and V. Narayanan, Switching of ferroelectric polarization in epitaxial BaTiO₃ films on silicon without a conducting bottom electrode, *Nat. Nanotechnol.* **8**, 748 (2013).
- [22] A. Rosa, D. Tulli, P. Castera, A. M. Gutierrez, A. Griol, M. Baquero, B. Vilquin, F. Eltes, S. Abel, J. Fompeyrine, and P. Sanchis, Barium titanate (BaTiO₃) RF characterization for application in electro-optic modulators, *Opt. Mater. Express* **7**, 4328 (2017).
- [23] G. H. Kwei, A. C. Lawson, S. J. L. Billinge, and S.-W. Cheong, Structures of the ferroelectric phases of barium titanate, *J. Phys. Chem.* **97**, 2368 (1993).
- [24] T. Paoletta and A. A. Demkov, Pockels effect in low-temperature rhombohedral BaTiO₃, *Phys. Rev. B* **103**, 014303 (2021).
- [25] J. E. Turney, E. S. Landry, A. J. H. McGaughey, and C. H. Amon, Predicting phonon properties and thermal conductivity from anharmonic lattice dynamics calculations and molecular dynamics simulations, *Phys. Rev. B* **79**, 064301 (2009).
- [26] T. Tadano and S. Tsuneyuki, Self-consistent phonon calculations of lattice dynamical properties in cubic SrTiO₃ with first-principles anharmonic force constants, *Phys. Rev. B* **92**, 054301 (2015).
- [27] K. Tsuda and M. Tanaka, Direct observation of the symmetry breaking of the nanometer-scale local structure in the paraelectric cubic phase of BaTiO₃ using convergent-beam electron diffraction, *Appl. Phys. Express* **9**, 71501 (2016).
- [28] M. S. Senn, D. A. Keen, T. C. A. Lucas, J. A. Hriljac, and A. L. Goodwin, Emergence of Long-Range Order in BaTiO₃ From Local Symmetry-Breaking Distortions, *Phys. Rev. Lett.* **116**, 207602 (2016).
- [29] M. Kotiuga, S. Halilov, B. Kozinsky, M. Fornari, N. Marzari, and G. Pizzi, Microscopic picture of paraelectric perovskites from structural prototypes, *Phys. Rev. Res.* **4**, L012042 (2022).
- [30] J. F. Nye, *Physical Properties of Crystals: Their Representation by Tensors and Matrices* (Oxford University Press, Oxford, 1985).
- [31] I. P. Kaminow and E. H. Turner, Electro-optic light modulators, *Appl. Opt.* **5**, 1612 (1966).
- [32] S. H. Wemple and M. DiDomenico Jr, Electro-optical and nonlinear optical properties of crystals, in *Applied Solid State Science*, Vol. 3 (Elsevier, New York, 1972), pp. 263–383.
- [33] M. Veithen, X. Gonze, and P. Ghosez, Nonlinear optical susceptibilities, raman efficiencies, and electro-optic tensors from first-principles density functional perturbation theory, *Phys. Rev. B* **71**, 125107 (2005).
- [34] A. K. Hamze, M. Reynaud, J. Geler-Kremer, and A. A. Demkov, Design rules for strong electro-optic materials, *npj Comput. Mater.* **6**, 130 (2020).
- [35] L. R. Dalton, P. Günter, and M. Jazbinsek, *Organic Electro-Optics and Photonics: Molecules, Polymers and Crystals* (Cambridge University Press, Cambridge, 2015).
- [36] I. P. Kaminow and W. D. Johnston Jr, Quantitative determination of sources of the electro-optic effect in LiNbO₃ and LiTaO₃, *Phys. Rev.* **160**, 519 (1967).
- [37] F. Detraux and X. Gonze, Photoelasticity of α -quartz from first principles, *Phys. Rev. B* **63**, 115118 (2001).
- [38] A. H. Romero, D. C. Allan, B. Amadon, G. Antonius, T. Applencourt, L. Baguet, J. Bieder, F. Bottin, J. Bouchet, E. Bousquet, F. Bruneval, G. Brunin, D. Caliste, M. Côté, J. Denier, C. Dreyer, P. Ghosez, M. Giantomassi, Y. Gillet, O. Gingras *et al.*, ABINIT: Overview, and focus on selected capabilities, *J. Chem. Phys.* **152**, 124102 (2020).
- [39] X. Gonze, B. Amadon, G. Antonius, F. Armandi, L. Baguet, J.-M. Beuken, J. Bieder, F. Bottin, J. Bouchet, E. Bousquet,

- N. Brouwer, F. Bruneval, G. Brunin, Théo Cavignac, J.-B. Charraud, W. Chen, M. Côté, S. Cottenier, J. Denier, Grégory Geneste *et al.*, The ABINIT project: Impact, environment and recent developments, *Comput. Phys. Commun.* **248**, 107042 (2020).
- [40] G. Kresse and J. Hafner, *Ab initio* molecular dynamics for liquid metals, *Phys. Rev. B* **47**, 558 (1993).
- [41] G. Kresse and J. Furthmüller, Efficiency of ab-initio total energy calculations for metals and semiconductors using a plane-wave basis set, *Comput. Mater. Sci.* **6**, 15 (1996).
- [42] G. Kresse and J. Furthmüller, Efficient iterative schemes for ab initio total-energy calculations using a plane-wave basis set, *Phys. Rev. B* **54**, 11169 (1996).
- [43] G. Kresse and J. Hafner, Norm-conserving and ultrasoft pseudopotentials for first-row and transition elements, *J. Phys.: Condens. Matter* **6**, 8245 (1994).
- [44] G. Kresse and D. Joubert, From ultrasoft pseudopotentials to the projector augmented-wave method, *Phys. Rev. B* **59**, 1758 (1999).
- [45] P. E. Blöchl, Projector augmented-wave method, *Phys. Rev. B* **50**, 17953 (1994).
- [46] D. M. Ceperley and B. J. Alder, Ground State of the Electron Gas by a Stochastic Method, *Phys. Rev. Lett.* **45**, 566 (1980).
- [47] J. P. Perdew and A. Zunger, Self-interaction correction to density-functional approximations for many-electron systems, *Phys. Rev. B* **23**, 5048 (1981).
- [48] M. Teter, Additional condition for transferability in pseudopotentials, *Phys. Rev. B* **48**, 5031 (1993).
- [49] H. J. Monkhorst and J. D. Pack, Special points for brillouin-zone integrations, *Phys. Rev. B* **13**, 5188 (1976).
- [50] B. Peng, Y. Hu, S. Murakami, T. Zhang, and B. Monserrat, Topological phonons in oxide perovskites controlled by light, *Sci. Adv.* **6**, 1618 (2020).
- [51] P. Souvatzis, O. Eriksson, M. I. Katsnelson, and S. P. Rudin, Entropy Driven Stabilization of Energetically Unstable Crystal Structures Explained From First Principles Theory, *Phys. Rev. Lett.* **100**, 095901 (2008).
- [52] I. K. Jeong, S. Lee, S. Y. Jeong, C. J. Won, N. Hur, and A. Llobet, Structural evolution across the insulator-metal transition in oxygen-deficient BaTiO_{3-δ} studied using neutron total scattering and rietveld analysis, *Phys. Rev. B* **84**, 064125 (2011).
- [53] W. Li, C. M. Landis, and A. A. Demkov, Evolution of epitaxial BaTiO₃ on SrTiO₃-buffered Si: Phase field analysis, *J. Appl. Phys.* **132**, 213103 (2022).
- [54] A. Scalabrin, A. S. Chaves, D. S. Shim, and S. P. S. Porto, Temperature dependence of the A₁ and E optical phonons in BaTiO₃, *Phys. Status Solidi B* **79**, 731 (1977).
- [55] G. Henkelman, B. P. Uberuaga, and H. Jónsson, A climbing image nudged elastic band method for finding saddle points and minimum energy paths, *J. Chem. Phys.* **113**, 9901 (2000).
- [56] Y. Xie, H. Yu, G. Zhang, and H. Fu, Lattice dynamics investigation of different transition behaviors of cubic BaTiO₃ and SrTiO₃ by first-principles calculations, *J. Phys.: Condens. Matter* **20**, 215215 (2008).
- [57] W. G. Schmidt, F. Bechstedt, and G. P. Srivastava, III-V (110) surface dynamics from an *ab initio* frozen-phonon approach, *Phys. Rev. B* **52**, 2001 (1995).
- [58] G. K. Horton and A. A. Maradudin, *Dynamical Properties of Solids: Disordered Solids, Optical Properties*, Vol. 4 (North-Holland Publishing Company, Amsterdam, 1980).
- [59] P. Hermet, M. Veithen, and P. Ghosez, Raman scattering intensities in BaTiO₃ and PbTiO₃ prototypical ferroelectrics from density functional theory, *J. Phys.: Condens. Matter* **21**, 215901 (2009).
- [60] A. Raeliarijaona and H. Fu, Mode sequence, frequency change of nonsoft phonons, and LO-TO splitting in strained tetragonal BaTiO₃, *Phys. Rev. B* **92**, 094303 (2015).
- [61] U. D. Venkateswaran, V. M. Naik, and R. Naik, High-pressure raman studies of polycrystalline BaTiO₃, *Phys. Rev. B* **58**, 14256 (1998).
- [62] Z. Z. Lazarević, N. Romčević, M. Vijatović-Petrović, N. Paunović, M. Romčević, B. D. Stojanović, and Z. Dohčević-Mitrović, Characterization of barium titanate ceramic powders by raman spectroscopy, *Acta Phys. Pol. A* **115**, 808 (2009).
- [63] M. D. Fontana, H. Idrissi, G. E. Kugel, and K. Wojcik, Raman spectrum in PbTiO₃ re-examined: Dynamics of the soft phonon and the central peak, *J. Phys. Condens. Matter* **3**, 8695 (1991).
- [64] K. D. Fredrickson, V. V. Vogler-Neuling, K. J. Kormondy, D. Caimi, F. Eltes, M. Sousa, J. Fompeyrine, S. Abel, and A. A. Demkov, Strain enhancement of the electro-optical response in BaTiO₃ films integrated on Si (001), *Phys. Rev. B* **98**, 075136 (2018).
- [65] T. Tadano, Y. Gohda, and S. Tsuneyuki, Anharmonic force constants extracted from first-principles molecular dynamics: applications to heat transfer simulations, *J. Phys.: Condens. Matter* **26**, 225402 (2014).
- [66] X.-G. Zhao, O. I. Malyi, S. J. L. Billinge, and A. Zunger, Intrinsic local symmetry breaking in nominally cubic paraelectric BaTiO₃, *Phys. Rev. B* **105**, 224108 (2022).
- [67] M. Zgonik, P. Bernasconi, M. Duelli, R. Schlessler, P. Günter, M. H. Garrett, D. Rytz, Y. Zhu, and X. Wu, Dielectric, elastic, piezoelectric, electro-optic, and elasto-optic tensors of BaTiO₃ crystals, *Phys. Rev. B* **50**, 5941 (1994).
- [68] S. Sanna, C. Thierfelder, S. Wipperfmann, T. P. Sinha, and W. G. Schmidt, Barium titanate ground-and excited-state properties from first-principles calculations, *Phys. Rev. B* **83**, 054112 (2011).
- [69] D. Berlincourt and H. Jaffe, Elastic and piezoelectric coefficients of single-crystal barium titanate, *Phys. Rev.* **111**, 143 (1958).
- [70] L. Chen, Y. Yang, Z. Gui, D. Sando, M. Bibes, X. K. Meng, and L. Bellaiche, Large Elasto-Optic Effect in Epitaxial PbTiO₃ Films, *Phys. Rev. Lett.* **115**, 267602 (2015).
- [71] D. Chelladurai, M. Kohli, Y. Horst, M. Eppenberger, L. Kulmer, T. Blatter, J. Winiger, D. Moor, A. Messner, C. Convertino, F. Eltes, Y. Fedoryshyn, and J. Leuthold, Electro-optic frequency response of thin-film barium titanate (BTO) from 20 to 270 GHz, in *European Conference and Exhibition on Optical Communication* (Optica, Basel, 2022), p. We5.72.
- [72] C. Kittel, *Introduction to Solid State Physics*, 5th ed. (Wiley, New York, 1976).
- [73] P. M. Dixit and U. S. Dixit, *Modeling of Metal Forming and Machining Processes: By Finite Element and Soft Computing Methods* (Springer Science & Business Media, New York, 2008).